Title: **Mode I Cohesive Law Characterization of Through-Crack Propagation in a Multidirectional Laminate**

Authors: Andrew C. Bergan
Carlos G. Dávila
Frank A. Leone
Jonathan Awerbuch
Tein-Min Tan

ABSTRACT

A method is proposed and assessed for the experimental characterization of through-the-thickness crack propagation in multidirectional composite laminates with a cohesive law. The fracture toughness and crack opening displacement are measured and used to determine a cohesive law. Two methods of computing fracture toughness are assessed and compared. While previously proposed cohesive characterizations based on the R-curve exhibit size effects, the proposed approach results in a cohesive law that is a material property. The compact tension specimen configuration is used to propagate damage while load and full-field displacements are recorded. These measurements are used to compute the fracture toughness and crack opening displacement from which the cohesive law is characterized. The experimental results show that a steady-state fracture toughness is not reached. However, the proposed method extrapolates to steady-state and is demonstrated capable of predicting the structural behavior of geometrically-scaled specimens.

INTRODUCTION

Structural failure of composite laminates occurs after the evolution and interaction of various damage mechanisms. Damage progression can be idealized at several length scales to model this behavior. Analyses have been proposed idealizing damage at the microscale [1], mesoscale [2], structural [3, 4], or some combination of scales [5]. For the case of a generic composite laminate structure

Andrew C. Bergan, FAA-Drexel Fellowship Student, Department of Mechanical Engineering and Mechanics, Drexel University, Philadelphia, PA 19104, U.S.A.
Carlos G. Dávila and Frank A. Leone, NASA Langley Research Center, Hampton, VA 23681, U.S.A.
Jonathan Awerbuch and Tein-Min Tan, Department of Mechanical Engineering and Mechanics, Drexel University, Philadelphia, PA 19104, U.S.A.

with a notch subjected to mode I loading, the following idealizations are common at each scale. At the microscale, fiber breaks and fiber-matrix debonds are observed and idealized. At the mesoscale, damage is often idealized as intralaminar cracks and delaminations between plies. At the structural scale, in-plane damage may coalesce into a through-the-thickness crack and delaminations may occur at structural interfaces. For progressive damage analysis, it is common and convenient to idealize damage at the mesoscale because the kinematics of the various damage mechanisms are influenced by the ply thickness and orientation [2]. However, for problems where no single mesoscale damage mechanism dominates the response, it may be sufficient to smear the effects of the micro- and mesoscale damage mechanisms and idealize damage at the structural scale. Structural scale damage idealization is desirable because significantly fewer degrees of freedom are required for macroscale representation compared with a mesoscale representation. One problem that has been idealized at the structural scale with some success is residual strength prediction of a notched composite structure [3, 4], which is a commonly used configuration in damage tolerance assessments [6]. For laminates with conventional stacking sequences under mode I dominant loading, the damage propagation from the notch is often collinear with the notch [7] and can be idealized as a through-crack.

In order to predict the propagation of a laminate through-crack accurately, it is necessary to consider the influence of various damage mechanisms such as matrix cracks, fiber breaks, and delamination acting at the micro- and mesoscale within a physical process zone of length, l_{FPZ}. The cohesive zone model (CZM) is commonly used for analyzing fracture initiation and propagation when the process zone is non-negligible [8–10]. The CZM represents the process zone as a zero thickness interface on which cohesive tractions, σ, are governed by a cohesive law

$$\sigma = \sigma(\delta) \tag{1}$$

which specifies σ in terms of the crack opening displacement, δ.

Cohesive laws of various forms have been suggested to be material properties and used to model the process zone with some success [11]. Under small-scale bridging (SSB) conditions, where l_{FPZ} is small compared with other length scales in the problem, a bilinear cohesive law

$$\sigma = K\delta \qquad 0 \le \delta < \frac{\sigma_c}{K} \tag{2a}$$

$$\sigma = -\frac{\sigma_c^2}{2G_c}\delta + \sigma_c \qquad \frac{\sigma_c}{K} \le \delta \le \frac{2G_c}{\sigma_c} \tag{2b}$$

is sufficient to model the fracture process, where K is the penalty stiffness, σ_c is the cohesive strength, and G_c is the fracture toughness [12]. The cohesive law comprises an initial linear segment (2a) with a high stiffness specified by the numerical parameter K and a softening segment (2b). The process zone length of a cohesive law, l_{FPZ}^c, can be approximated as

$$l_{\mathrm{FPZ}}^c = \gamma \frac{E G_c}{\sigma_c^2} \tag{3}$$

where, for isotropic materials, E is the Young's Modulus and γ is a nondimensional parameter that depends on the specific model. However, bilinear cohesive laws have been unable to predict laminate through-crack propagation uniformly and accurately (see e.g. [3, 4, 12, 13]).

The importance of the shape of the cohesive law for predicting laminate through-crack propagation suggests that large scale bridging (LSB) conditions dominate. Under LSB, where l_{FPZ} is large compared with relevant length scales, the shape of the softening law is fundamental and must be represented accurately [14–17]. Laminate through-crack process zone lengths have been observed experimentally to be several times the laminate thickness [18]. The relation between the cohesive law shape and the structural response was studied with parametric finite element (FE) analyses in reference [4] and it was concluded that a cohesive law with convex softening can predict through-crack propagation accurately for a variety of configurations.

An inexpensive and reliable experimental method for characterizing the cohesive law is needed. Cohesive law characterization procedures have been demonstrated for delamination under mode I and mode II loading where LSB conditions prevail [17, 19]. These methods were derived such that the cohesive law is guaranteed to be a material property [16, 17]. In contrast, the state-of-the-art method for cohesive law characterization of a through-crack, reference [12], is based on the crack growth resistance curve, or R-curve, which is a structural property under LSB conditions. Therefore, the existing method cannot be expected to yield a cohesive law that is a material property if the l_{FPZ} is large. The objective of this work is to introduce and demonstrate a general method for characterizing the cohesive law of a laminate through-crack under mode I loading. A secondary objective is assess the suitability of two data reduction methods to compute fracture toughness, namely, the J-integral method and the modified compliance calibration (MCC) method.

The remainder of this paper is organized as follows. The next section reviews two methods for calculating the R-curve and assesses the existing fracture-based method of determining a cohesive law for a through-crack using the R-curve. The following section demonstrates the adaptation of Sørensen and Jacobsen's method [17] that is proposed for cohesive law characterization of laminate through-cracks. The proposed method is verified numerically and approximations introduced for experimental convenience are shown to contribute only minor error to the cohesive characterization. Next, this method is applied experimentally for a particular laminate that is a candidate for use in the skin of future aerospace structures. Results are compared for two specimen sizes to examine the scalability of the cohesive characterization.

THE R-CURVE

Recently, emphasis has been placed on determining the R-curve for intralaminar fiber fracture of an *in-situ* ply to be used as input for mesoscale progressive damage models [20]. The cross-ply compact tension (CT) specimen proposed by Pinho et al. [21] has been applied with some success and a method has been developed to quantify a trilinear cohesive law based on a measured R-curve [12]. The basic

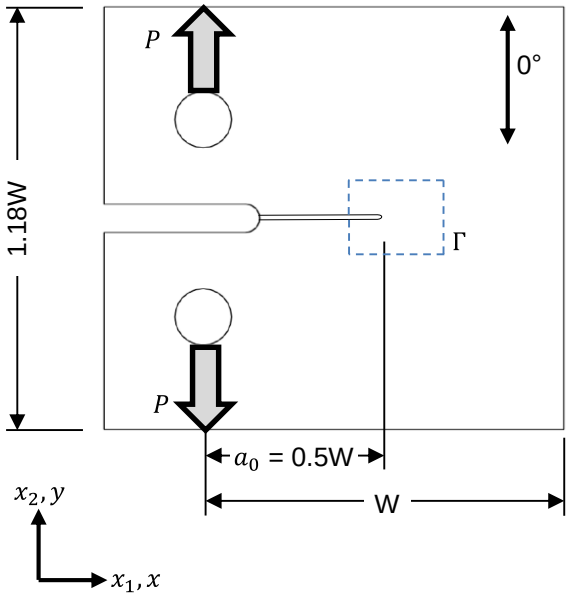

Figure 1. Composite CT specimen configuration

geometry of the CT specimen is shown in Figure 1. The specimen proposed by Pinho et al. has a width W=2.01 inches and a thickness of 0.156 inches. Several data reduction procedures were proposed and compared in references [21, 22]. The two preferred methods of determining the R-curve from CT tests are reviewed in the following sections: the J-integral method [23, 24] and the MCC method [12, 21, 25].

J-Integral Method

The J-integral method can be used to determine the fracture toughness at increments of crack growth by computing Rice's J-integral [26] around a contour enclosing the process zone using displacement data obtained from digital image correlation (DIC). The J-integral is

$$J = \int_{\Gamma} \left(w dx_2 - \mathbf{t} \cdot \frac{\partial \mathbf{u}}{\partial x_1} ds \right) \tag{4}$$

where the x_1 direction is aligned with the crack propagation direction, Γ is a contour chosen within the elastic region such that it encloses the inelastic process zone (example shown in Figure 1), w is the strain energy density, $\mathbf{t}$ is the traction vector, and $\mathbf{u}$ is the displacement field. The strain and displacement data are obtained from DIC data and the stresses are computed from strains using classical lamination theory. The R-curve, $J_R(\Delta a)$, is obtained by computing the contour integral (4) at several increments of crack growth, Δa. The crack length can be measured visually [22], identified from correlation measurements computed by DIC [23], or by using equation (4) in conjunction with the M-integral [24], which is a contour integral derived in reference [27] to extract the mode I and mode II stress

intensity factors from the total energy release rate. The advantage of the J-integral method is that it completely characterizes the effect of the process zone and intrinsically contains the softening law. However, the J-integral method is cumbersome to apply because the contour that encloses the entire inelastic region is often unclear without complementary inspection to assess the extent of damage.

The MCC Method

In contrast to the J-integral method, which allows for arbitrary inelastic behavior at the notch tip, the MCC method is derived assuming linear elastic fracture mechanics (LEFM) conditions at the crack tip. The MCC method computes the strain energy release rate, G, with the well-known equation [25, 28]

$$G = \frac{P^2}{2t}\frac{\partial C}{\partial a} \tag{5}$$

where P is the applied load, t is the thickness, $C = \delta_l/P$ is the specimen compliance where δ_l is the opening displacement measured along the load line, and a is the crack length. When a crack is characterized accurately with LEFM, $J = G$. However, in general $J \neq G$ when the process zone size is non-negligible [16].

While no assumptions of the conditions at the crack tip are included in equation (5), practical application requires

$$C = C(a) \tag{6}$$

which inherently requires some assumption of the crack tip conditions as they effect the compliance. Often equation (6) is derived theoretically, approximated from a numerical model, or determined experimentally. In all cases, the effect of the process zone on compliance is ignored (e.g. [22, 25]), which is a valid assumption under SSB conditions. However, ignoring the effect of cohesive tractions on compliance is strictly invalid for arbitrary cohesive laws under LSB conditions [16], [17, 29]. Tamuzs et al. examined this assumption using FE in which a cohesive law was assumed such that LSB conditions prevailed [30]. It was demonstrated that when equation (5) is written as a function of P and δ_l so that crack length is eliminated from the expression, the resulting G_R was in good agreement with J_R.

In order to apply equation (5) to an orthotropic CT specimen, Dávila et al. proposed a curve fit for equation (6) based on a FE model because a theoretical solution is unavailable [12]. Three fit parameters, α, β, and χ, were selected so that

$$C = \frac{\delta_l}{P} = (a\alpha + \beta)^{-1/\chi} \tag{7}$$

fit the numerical model results for a range of crack lengths. Substituting equation (7) into equation (5)

$$G = \frac{P^2}{2t}\frac{\alpha\left(C^{-\chi}\right)^{-\left(1+\frac{1}{\chi}\right)}}{\chi} \tag{8}$$

which is convenient in that it eliminates the need for a visually measured crack length, which is difficult to discern consistently and accurately. Rearranging (7), an effective crack length, a_{eff}, can be obtained

$$a_{\text{eff}} = \frac{1}{\alpha}(C^{-\chi} - \beta) \tag{9}$$

where it is noted that a_{eff} lies within the process zone. Some error is introduced in equation (8) when the fit for equation (6) is based on a linear FE model because the expression for equation (6) ignores the contribution of the cohesive tractions to the compliance. Therefore, the MCC method should be recognized as an approximation in contrast to the J-integral method, which introduces no such assumptions. The primary benefit of the MCC method compared to the J-integral method is its simplicity.

Comparison of the J-integral and MCC methods

A parametric FE model of the CT specimen was used to assess the accuracy of the MCC method compared with the J-integral method. In addition, the effect of specimen size was considered. The model was developed in Abaqus using four node 2D continuum elements [31]. The same specimen configuration as in references [12, 21] was used (Figure 1): the initial specimen width was $W_0 = 2.01$ inches; the layup was $[90/0]_{8s}$ with a ply thickness of 0.0049 inches; and the ply properties were $E_1 = 19.10$ Msi, $E_2 = 1.28$ Msi, $G_{12} = 6.67$ Msi, and $\nu_{12} = 0.32$. A row of superposed, zero-thickness, four-node cohesive elements (COH2D4) was placed ahead of the notch tip and the trilinear cohesive law from reference [12] was used with $G_c = 1028$ lbf/inch, $\sigma_c = 218$ ksi, $m = 0.556$, and $n = 0.866$. As in reference [12], the superposed bilinear cohesive laws, a and b, were defined as

$$G_c^a = mG_c;\ \sigma_c^a = n\sigma_c;\ K^a = nK \tag{10a}$$

$$G_c^b = (1-m)G_c;\ \sigma_c^b = (1-n)\sigma_c;\ K^b = (1-n)K \tag{10b}$$

such that maximum cohesive stresses occur at the same opening displacement as shown in Figure 2 [12].

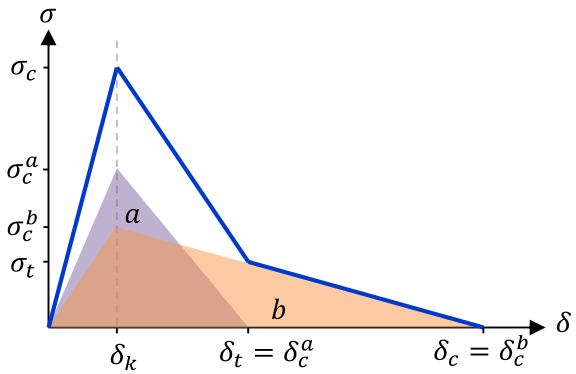

Figure 2. Trilinear cohesive law formed by superposing two bilinear cohesive laws

The material properties listed above are identical to those used in reference [12] except σ_c and n, which were updated based on more recent test data.

The R-curves calculated using the J-integral and MCC methods from the numerical model are shown in Figure 3 for three specimen sizes. The specimen width, W, was increased while keeping the cohesive element length constant. The MCC method was computed using equation (8) while the J-integral was computed using the domain integration method (built-in to Abaqus) because it is more accurate than direct numeric implementation of the contour integral [32]. The change in crack length, Δa, was measured from the initial notch to the farthest damaged element. The stair-step behavior for $\Delta a < 0.1$ is due to the element size; smaller elements would smooth this nonphysical effect. It is observed in Figure 3 that the MCC method yields a relatively close approximation of the J-integral result for all three specimen sizes.

The results in Figure 3 also show that both the MCC and J-integral methods predict the fracture process zone length measured from the initial crack length to where the R-curve reaches a steady-state, l_{FPZ}^{s}, increases with the specimen size. The dependence of l_{FPZ}^{s} on specimen size is likely due to the changing influence of the compressive region at the back edge on the process zone and, to a lesser degree, specimen compliance. It is important to recall that the cohesive law is assumed to be a material property whereas, under LSB conditions, the R-curve and l_p are influenced by the structure. This was theoretically postulated by Suo [16] and demonstrated experimentally and numerically for DCB specimens under LSB conditions by Sørensen and Jacobsen [17]. The numerical results in Figure 3 demonstrate the same behavior for the CT configuration, namely, that the l_{FPZ}^{s} and the R-curve are structural properties. The results suggests that LSB conditions should be considered in analysis and characterization of through-crack propagation in composite laminates.

Dávila et al. proposed a definition for m and n based on the experimentally measured R-curve as

$$m = \frac{G_c^a}{G_c} \tag{11}$$

$$n = 1 - (1 - m)\frac{2l_{\mathrm{FPZ}}^{c}}{3l_{\mathrm{FPZ}}^{s}} \tag{12}$$

where G_c^a is the initiation fracture toughness. The cohesive law is thus defined by G_c, σ_c, G_c^a, and l_{FPZ}^{s}. Clearly, this model is not appropriate to characterize the cohesive law here because the sensitivity of l_{FPZ}^{s} to the specimen size (Figure 3) indicates each specimen size yields a different cohesive law. In other words, the numerical analysis results suggest n varies with specimen size, yet the same cohesive law was used as input to define the model for all three sizes. The significance of this deficiency is that the methodology to extract a cohesive law from experimental R-curves using equations (10)-(12) does not result in a unique set of material properties when LSB conditions prevail.

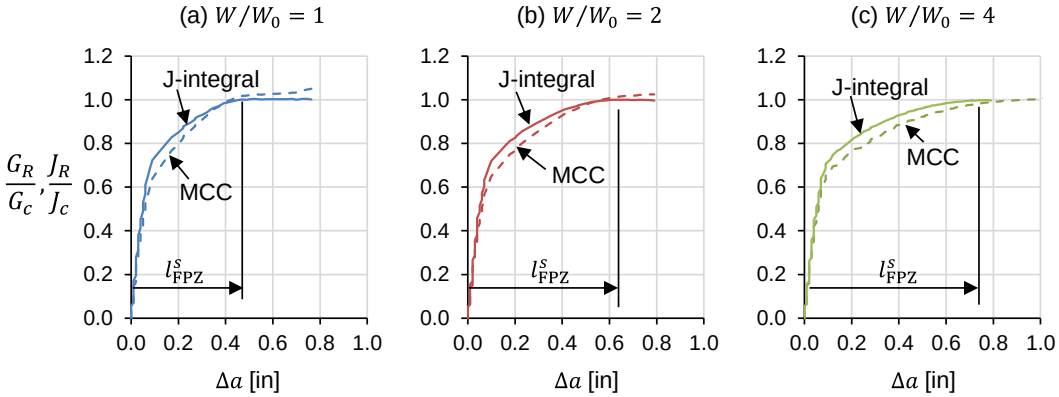

Figure 3. Comparison of the R-curve determined by the J-integral and MCC methods using geometrically scaled numerical models. The effect of specimen size on l^s_{FPZ} is highlighted.

COHESIVE LAW CHARACTERIZATION

An expression for the cohesive law in terms of J_R was obtained by Suo et al. as follows [33]. The J-integral (4) is evaluated around a cohesive crack

$$J_R = \int_0^{\delta_c} \sigma(\delta) d\delta \tag{13}$$

where δ_c is the critical opening at which a traction free crack is formed. Differentiating equation (13) with respect to δ gives the cohesive law

$$\sigma(\delta) = \frac{\partial J_R}{\partial \delta} \tag{14}$$

Suo et al. suggested that (14) could be used to characterize the cohesive law. Subsequently, other authors have done so for specimen configurations in which a closed-form solution for the J-integral is available [17, 19].

Proposed Cohesive Law Characterization Method

As an alternative to computing the J-integral, the MCC method can be used in equation (14) if $G_R = J_R$ is assumed, in which case equation (14) is replaced by

$$\sigma(\delta) = \frac{\partial G_R}{\partial \delta} \tag{15}$$

which is a convenient basis for characterizing a though-crack cohesive law. As stated above, the MCC method is preferred to the J-integral method for its relative simplicity. For experimental application, δ can be measured easily using DIC without the unique experimental setup used in [17].

In practical application, it is beneficial to fit the $G_R(\delta)$ data to an analytic expression derived in terms of parameters that have physical significance. The analytic fit is differentiated in equation (15) instead of differentiating the $G_R(\delta)$ data numerically. The primary benefit of curve fitting the $G_R(\delta)$ data is that a set of meaningful parameters that define the cohesive law are obtained. However, the curve fit must be sufficiently general and representative of the test data. A cohesive law with concave softening, similar to the trilinear cohesive law shown in Figure 2, was shown capable of representing the softening behavior observed in a variety of laminates through parametric experimental investigation [4].

An expression for the trilinear cohesive law is formulated and integrated in order to fit the $G_R(\delta)$ data. The trilinear cohesive law is defined as

$$\sigma(\delta) = \begin{cases} \sigma_1(\delta) & 0 \le \delta \le \delta_k \\ \sigma_2(\delta) & \delta_k < \delta \le \delta_t \\ \sigma_3(\delta) & \delta_t < \delta \le \delta_c \end{cases} \tag{16}$$

where

$$\sigma_1(\delta) = K\delta \tag{17a}$$

$$\sigma_2(\delta) = \frac{n\sigma_c(\sigma_t - \sigma_c)}{2mG_c}\delta + \sigma_c \tag{17b}$$

$$\sigma_3(\delta) = \frac{\sigma_c^2(n-1)^2}{2G_c(m-1)}\,\delta + (1-n)\sigma_c \tag{17c}$$

where, for the purpose of formulating $\sigma_2(\delta)$ and $\sigma_3(\delta)$, it is assumed that $K \gg \sigma_c$ and therefore $\delta_k \approx 0$. For the purpose of the curve fit, $\sigma_1(\delta)$ can be ignored because it is independent of the four parameters that define the cohesive law (G_c, σ_c, m, and n) and $\delta_k \approx 0$. The stress at the transition between $\sigma_2(\delta)$ and $\sigma_3(\delta)$ is

$$\sigma_t = \frac{\sigma_c(n-1)(n-m)}{n(m-1)} \tag{18}$$

Substituting (17) into (13) and integrating yields

$$J_{\text{fit},2}(\delta) = \frac{n\sigma_c(\sigma_t - \sigma_c)\delta^2}{4mG_c} + \sigma_c\delta + C_1 \tag{19a}$$

$$J_{\text{fit},3}(\delta) = \frac{\sigma_c^2(n-1)^2\delta^2}{4G_c(m-1)} + (1-n)\sigma_c\delta + C_2 \tag{19b}$$

where $C_1 = 0$ assuming $J_{\text{fit},1}(\delta_k) \approx 0$ and C_2 is specified so that $J_{\text{fit},2}(\delta_t) = J_{\text{fit},3}(\delta_t)$ to enforce continuity in $J_{\text{fit}}(\delta)$. Equation (19) can be fit to the test data by selecting G_c, σ_c, m, and n such that the residual, η, is minimized

$$\eta = \sum_{i}^{n_s} \left| J_{\text{fit}}^{i} - G_R^{i} \right| \tag{20}$$

where n_s is the number of data points, J_{fit}^{i} is the analytic fracture toughness computed for data point i, and G_R^i is the value of fracture toughness for data point i. The four parameters that define the cohesive law, G_c, σ_c, m, and n, are thus characterized by fitting (19) to the measured $G_R(\delta)$ data.

Numerical Verification

The FE model of the CT specimen with the trilinear cohesive law described above was used to assess the proposed cohesive law characterization methodology. Both the J-integral and MCC methods were considered with the aim of quantifying the error introduced when using the MCC method compared to the J-integral method. Based on equation (14), it seems appropriate to plot J_R vs. δ as proposed in reference [17], instead of the conventional R-curve plot of J_R vs. Δa. Plotting J_R vs. δ is preferable to J_R vs. Δa because of the inherent ambiguity of the crack tip location within large process zones and the dependence of process zone length on specimen compliance as was shown in Figure 3. Figure 4 shows normalized fracture toughness as a function of normalized crack tip opening for both the J-integral and MCC methods. The J-integral results were nearly identical for all three specimen sizes as expected, and therefore shown by the single solid line. The MCC method generated slightly different results for each specimen size, denoted by the broken lines. The MCC method underpredicts the fracture toughness as the fracture process zone develops and overpredicts the steady-state fracture toughness by 2%. The discrepancy between G_R and J_R in Figure 4 is quite similar to that observed in Figure 3.

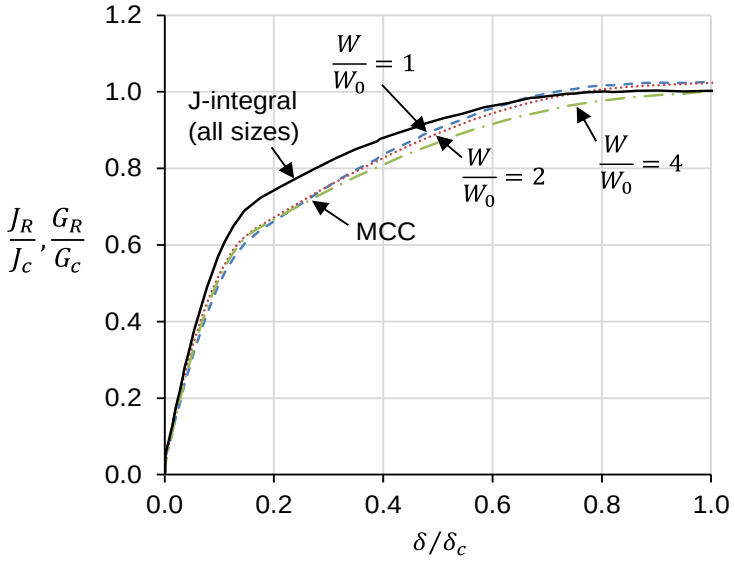

Figure 4. Fracture toughness vs. crack tip opening displacement computed by the J-integral and MCC methods for different specimen sizes

The proposed cohesive law characterization methodology was applied to the results from the numerical model. The accuracy of the cohesive law characterization was quantified through comparison to the cohesive law defined in the model input. For verification, the J-integral method was considered as well (J_R instead of G_R is used in the second term of equation (20)). Figure 5a shows a comparison of the cohesive laws. Using both the J-integral and MCC methods, a good approximation of the input cohesive law is obtained. However, the J-integral method is slightly better than the MCC method. The load vs. displacement responses predicted by the cohesive law characterizations also help to quantify the procedure accuracy. Figure 5b shows that the cohesive law characterized using the J-integral reproduced the load vs. displacement nearly identically to the original model. The load vs. displacement prediction from the cohesive law characterized using the proposed method (with MCC) underestimated the peak load by 6.9%. This relatively small error indicated that the proposed approach is an acceptable approximation. The characterized cohesive law parameters and corresponding percent error are summarized in Table I.

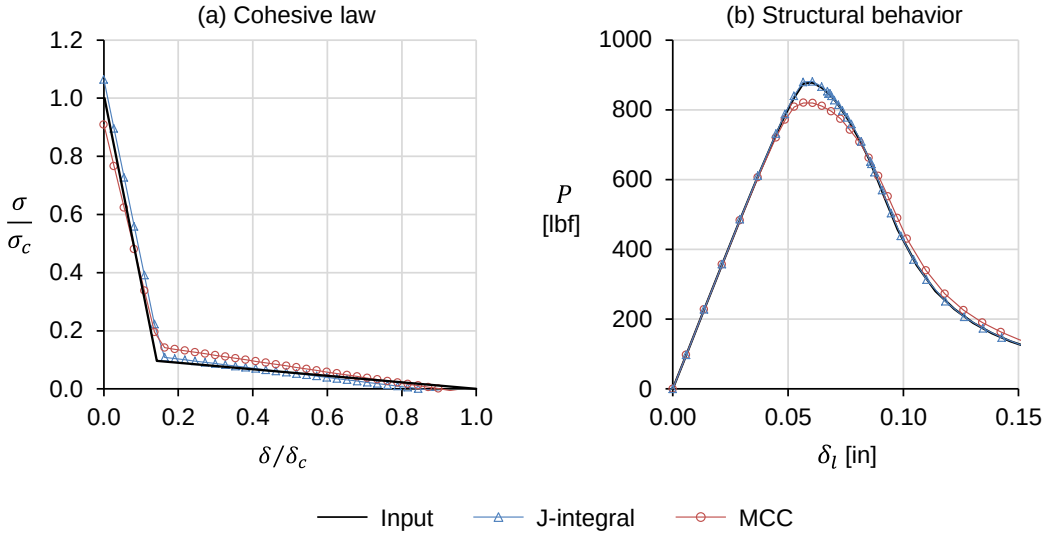

Figure 5. Verification of cohesive law characterization

TABLE I. CHARACTERIZED COHESIVE LAW PARAMETERS

		σ_c [ksi]	G_c [lbf/in]	m	n
J-integral	Value	231500	1031	0.5561	0.8736
	Error	6.4%	0.3%	0.01%	-1.4%
MCC	Value	197804	1053	0.4069	0.8097
	Error	-9.1%	2.5%	-26.8%	-8.6%

Measurement of δ

The proposed cohesive law characterization is sensitive to the location at which δ is measured. Theoretically, δ is measured across the cohesive interface at the notch tip. For experimental application, δ is measured between the two points shown in Figure 6a, which are initially separated by a nonzero distance, s. When using DIC, displacement data is not computed immediately at the notch tip because such edge data is unreliable. Thus, the DIC-measured crack tip opening displacement, δ_{DIC}, is taken at points with $s > 0$ where the particular value of s is related to the subset size. The FE model introduced above was used to investigate the effect of s on the $J_R(\delta_{DIC})$ and the results are shown in Figure 6b. For $s \approx 0$, J_R rises nearly vertically due to the cohesive element penalty stiffness, after which the curve is approximately linear with a slope equal to the cohesive strength. In contrast, when $s > 0$, J_R resembles a convex parabolic curve before reaching a linear range with the same slope as when $s \approx 0$. Therefore, δ_{DIC} should be offset so that the initial nonlinearity is removed such that

$$\delta = \delta_{\mathrm{DIC}} + b/\mu \tag{21}$$

where b is the intercept and μ is the slope of a line fit through the linear portion of the $J_R(\delta_{\mathrm{DIC}})$ curve.

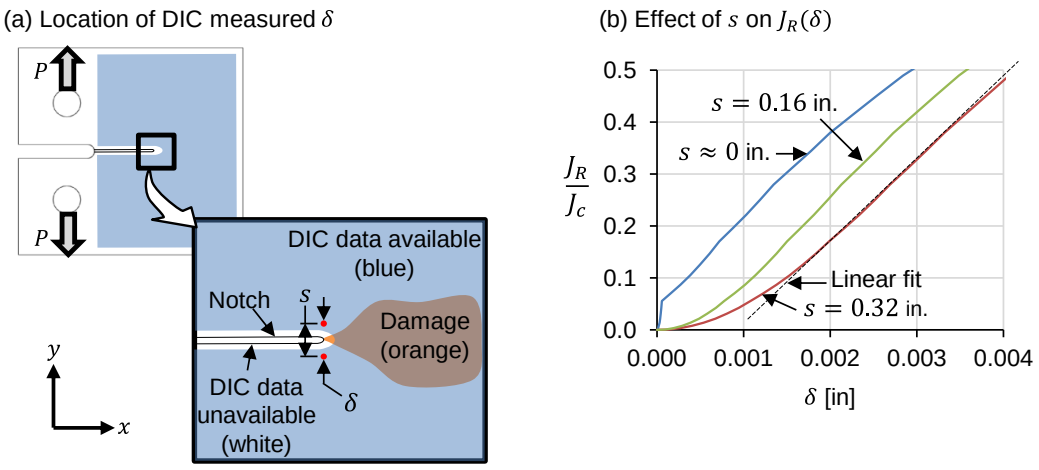

Figure 6. Predicted effect of crack opening displacement measurement location on $J_R(\delta)$

Experimental Procedure

The proposed approach was used for experimental characterization of the cohesive law of a thin multidirectional laminate. Specimens of two sizes were fabricated from flat panels with the configuration shown in Figure 1 following the standard used for testing metals [37], as proposed for composites by Pinho et al. [21]. The purpose of the larger specimens was to validate that a cohesive law characterized using the small specimens is capable of predicting the behavior of larger structures. The specimens are designated 'S' and 'L' for small (W = 2.01 in.) and large (W = 4.02 in.), respectively. Figure 7 shows a photograph of a typical specimen of each size. All specimens had a $[\pm 45/90_2/0/90_2/\pm 45]_s$ layup with a laminate thickness of 0.104 inches. The material comprised AS4 fibers formed as a non-crimp fabric and VRM-34 resin infused and oven-cured. The notch was machined in two steps. For convenience, a 0.16-inch-wide notch was machined for the majority of the notch length. The notch was extended to the length $a_0 = W/2$ with an abrasive slurry wire saw, using a 0.005-inch-diameter wire. The geometry of 'S' is identical to that of reference [21] except that the ratio of the length of the fine notch to the wide notch is larger, which may help suppress damage at the wide notch tip observed in some previous CT tests.

Five replicates of both sizes were tested under displacement control at a loading rate of 0.01 and 0.02 inches per minute for the small and large specimens, respectively. Load was recorded with a 5 kip load cell. Full-field displacements were recorded using VIC-3D [38].

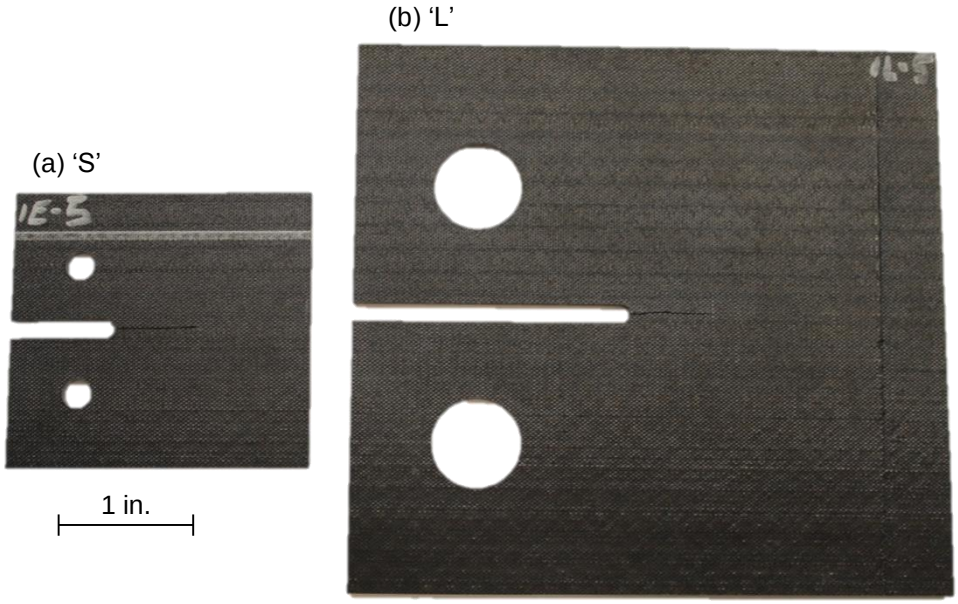

Figure 7. Photograph of typical CT specimens

Anti-Buckling Guide

A limitation of the CT configuration is the susceptibility for buckling when the thickness is small and the fracture toughness is high. While the specimen thickness has been selected to preclude buckling in previous tests of cross ply laminates [34], the multidirectional laminate of interest here is relatively thin as is typical for fuselage skins. Catalanotti et al. [35] proposed a method using a series of geometrically scaled double edge notched specimens as an alternative to the CT configuration largely because of buckling. If buckling can be suppressed, the CT configuration is desirable because only a single specimen is required to characterize the cohesive law. For fracture toughness testing of metals, buckling is prevented with Teflon coated plates that loosely sandwich the specimen [36]. For the present tests, an alternative anti-buckling design was developed and employed to minimize contact with the specimen and thus limit interaction with developing damage. The anti-buckling guide is shown schematically in Figure 8a. The two pieces of the anti-buckling guide clamp the back edge of the specimen and were constrained so that $u_z = 0$ at the far end. It addition, shims were used between the clevises and specimen to center the specimen within the clevises and prevent local buckling.

A FE model of the specimen and anti-buckling guide was used to verify all buckling modes were suppressed for the applied displacement range anticipated during the test. The specimen was modeled with shell elements and the anti-buckling guide was modeled with beam elements in Abaqus [31]. A kinematic coupling constraint was used to constrain the clamped portion of the CT specimen

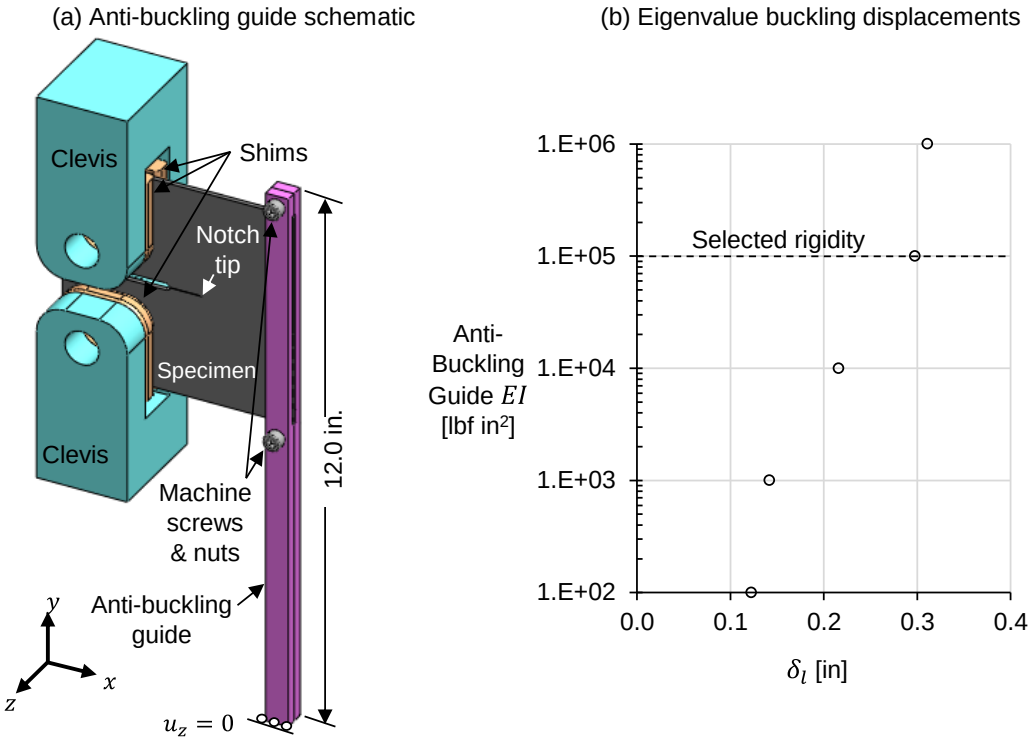

Figure 8. Anti-buckling guide schematic and FE results used to size the guide

to the anti-buckling guide. The flexural rigidity of the anti-buckling guide was varied and the eigenvalue buckling displacements were recorded. Figure 8b summarizes the results for the large specimens. Based on these results, an anti-buckling guide with bending stiffness of $EI = 1 \text{ x } 10^5$ lbf-in^2 was chosen. This stiffness ensured all buckling was suppressed to a displacement 1.5 times the peak anticipated displacement in the test. It is noted that higher flexural rigidity yields diminishingly higher displacement capability, such that larger CT specimens would be impractical for this particular laminate.

Test and Analysis Results

The load vs. displacement test results show relatively low scatter with consistent peak load levels. The load vs. load-line displacement results for both specimen sizes are shown in Figure 9. Visually observed damage initiation loads correspond with deviations from linearity in the load vs. displacement record, as shown for one large specimen in Figure 10. Damage was first observed as a splitting crack oriented along the 45°-direction, parallel to surface ply orientation. The DIC coefficient correlation, or measure of how a well a pixel is correlated between the images from the two cameras, indicated damage by poor correlation compared to the surrounding region. Damage propagated slowly and stably with the stick-slip behavior characteristic of fracture in composite laminates. Catastrophic failure occurred due to compressive failure at the back edge and so all results were truncated prior to indication of compressive failure.

Out-of-plane displacements were monitored using DIC and found to be small for all specimens. The deformed shapes observed resembled the buckling modes determined by analysis. However, the deformation occurred slowly and uniformly as load increased and was small in magnitude suggesting it was due to misalignment.

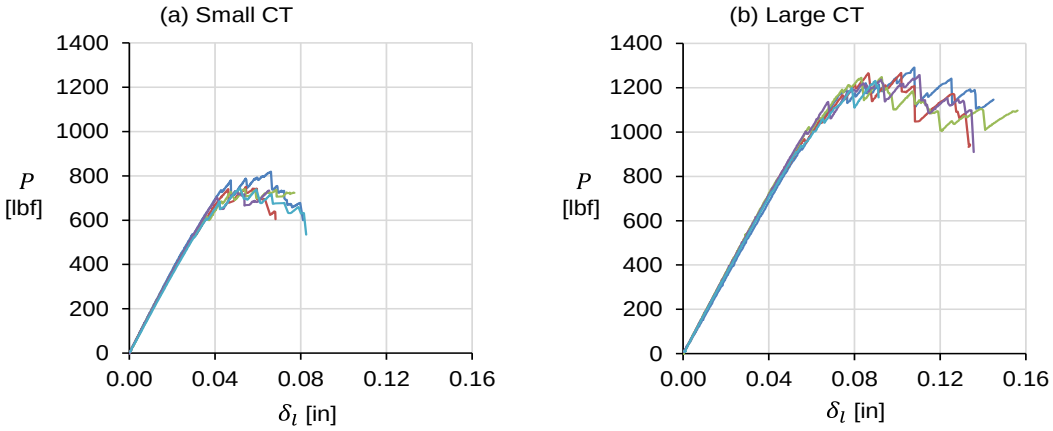

Figure 9. Measured load vs. displacement for the small and large CT specimens showing all replicates

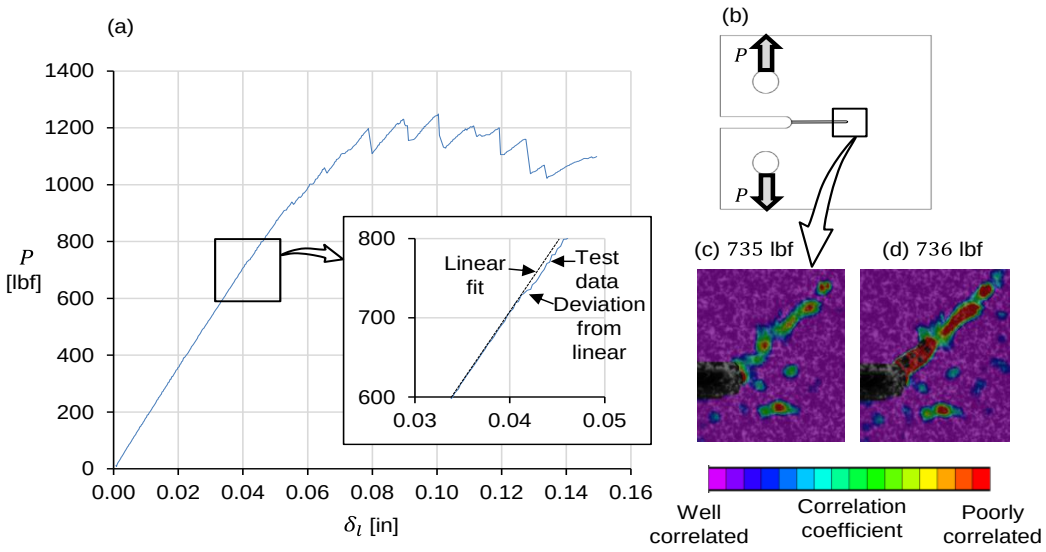

Figure 10. Damage initiation for one large specimen as observed in the load vs. displacement record, visually, and via the DIC correlation coefficient

The R-curves were computed using the MCC method (8) and are shown in Figure 11, where the abscissa is the effective crack length, Δa_{eff}, computed using (9). The J-integral (4) was computed for one specimen at five stages of damage growth and the results were found to agree well with the MCC method, as shown with the black circles in Figure 11a. It is observed that the R-curves for the small and large specimens are consistent, with the large specimens providing more damage propagation prior to catastrophic failure. The results do not give an indication of the R-curve reaching steady-state. Since no steady-state fracture toughness is reached, it is not possible to ascertain a process zone length from these results, and so the cohesive characterization method proposed in [12] is inapplicable.

Figure 12 shows G_R computed with the MCC method vs. notch tip opening displacement measured with DIC. It is observed that the results from the small and large specimens are consistent. The behavior of G_R can be segmented into two distinct ranges of δ. For $\delta \leq \delta_t$, the results are concave as softening initiates. For $\delta > \delta_t$, the curvature is smaller but remains concave. In these tests, $\delta_t \approx 0.008$ inches. These results suggest a piecewise linear cohesive law with convex softening is appropriate because the corresponding piecewise quadratic $G_R(\delta)$ can approximate the test data well.

The proposed cohesive law characterization procedure was applied considering two sets of test data. In the first case, $J_{\text{fit}} = J_{\text{fit,all}}$, test data from both the small and large specimens were used in (20). In the second case, $J_{\text{fit}} = J_{\text{fit,sm}}$, test data from only the small specimens were used in (20) for the purpose of demonstrating that the cohesive law characterization can predict the behavior in larger specimens accurately (i.e. the cohesive law is a material property). The results obtained from the two characterizations are compared in the following.

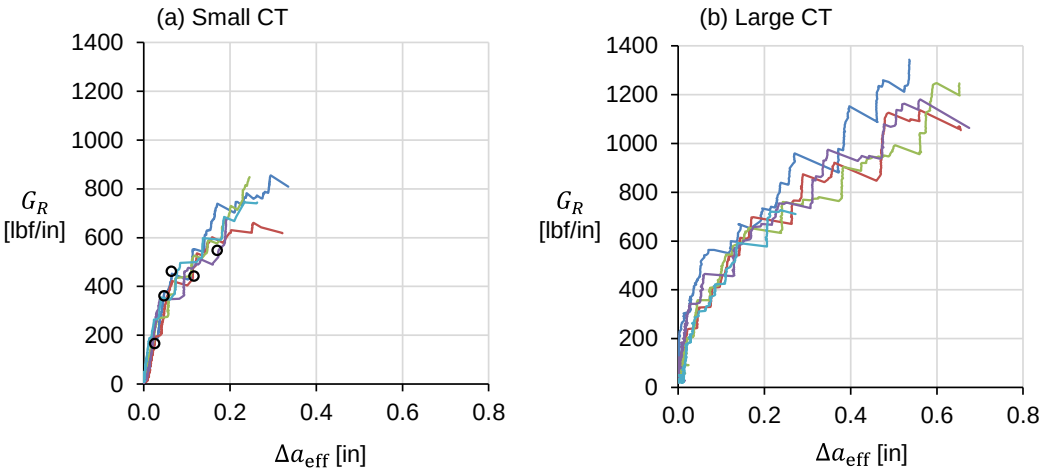

Figure 11. Experimentally measured R-curves where the solid lines are computed using the MCC method (8) and the black circles are computed using the J-integral method (4)

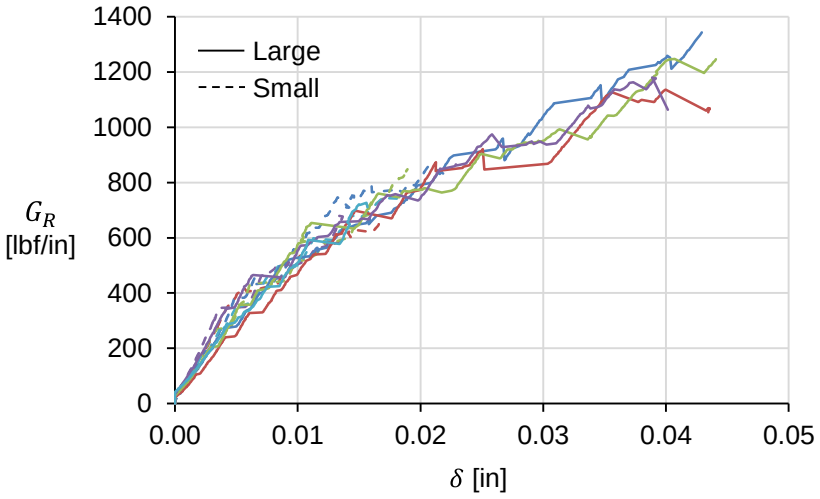

Figure 12. Experimentally measured fracture toughness vs. notch opening displacement

For cases where the test results yield a steady-state fracture toughness, the cohesive law can be completely characterized by the test data and the extension to larger structures is clear. However, in cases such as the present, where the steady-state fracture toughness was not reached during the test, the cohesive characterization must be extrapolated to a steady-state. Therefore, it is instructional to examine the application to larger structures in which the extrapolated portion of the cohesive law is significant. This is done here by comparing the extrapolated characterization, $J_{\text{fit,sm}}$, to the characterization of all specimens, $J_{\text{fit,all}}$. Both characterizations are plotted (black lines) in Figure 13 over the test data (grey lines) where the broken lines correspond to the small specimens. Both fits generally represent the test data well, though it is noted that $J_{\text{fit,sm}}$ is near the upper bound of the test data in the extrapolated region ($\delta > 0.02$ in.). The fit parameters are summarized in Table II.

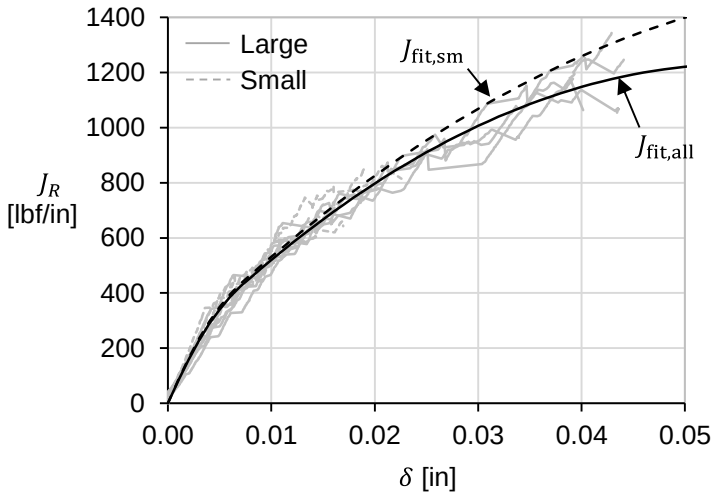

Figure 13. Analytic fits (black lines) of the measured fracture toughness

TABLE II. EXPERIMENTALLY CHARACTERIZED COHESIVE LAW PARAMETERS

Specimen Set	σ_c [ksi]	G_c [lbf/in]	m	n
all	87310	1231	0.142	0.566
small	89894	1522	0.123	0.586

The two characterized cohesive laws are plotted in Figure 14. The primary difference between the cohesive law obtained by fitting to all specimens compared with fitting to the small specimens only is δ_c.

The accuracy of the load vs. displacement behavior predicted from the characterized cohesive laws is obtained by analyzing FE models with the experimentally determined cohesive laws for both specimen sizes. The results are shown in Figure 15. Both characterizations predict the structural response within the scatter of the experimental data. While the characterization based on the small specimens trends toward the upper bound of the experimental, the overall

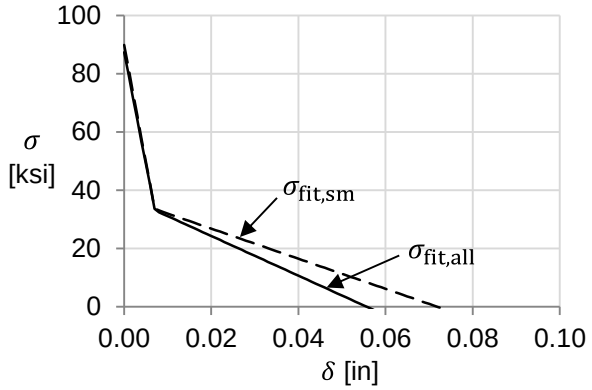

Figure 14. Experimentally characterized cohesive laws

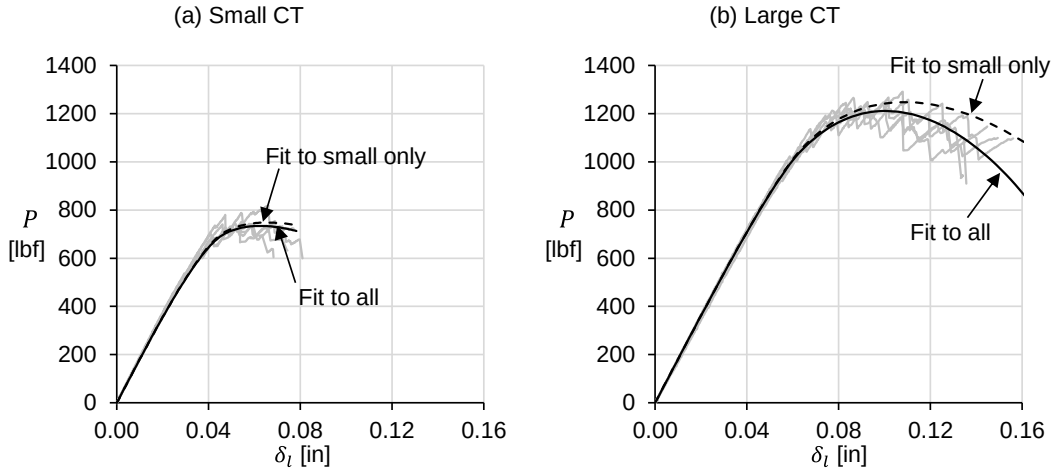

Figure 15. Load vs. displacement test and analysis results

agreement is quite good. These results suggest that mode I through-crack fracture in this laminate can be characterized accurately with a trilinear cohesive law even when the steady-state fracture toughness is not reached during the test.

CONCLUDING REMARKS

Results are presented that confirm that the R-curve and process zone length should not be considered material properties under large-scale bridging because of their dependence on structural compliance for composite laminate through-crack propagation in the CT configuration. Therefore, the experimental method for cohesive law characterization presented by Sørensen and Jacobsen in reference [17], in which the cohesive law is obtained as the derivative of the J-integral with respect to the crack tip opening displacement, should be used instead of methods based on the R-curve. Full-field displacement measurement using digital image correlation enables straightforward application of this method with a conventional compact tension configuration for characterization of a cohesive law for through-the-thickness crack propagation. The modified compliance calibration method can be used instead of the J-integral method for convenience with only a small (conservative) error introduced.

The test results reported here show no indication of reaching a steady-state fracture toughness prior to catastrophic failure. An assumed analytical trilinear cohesive law was derived and fit to the test data such that fracture toughness was extrapolated to a steady-state. The characterized cohesive law predicted the structural response accurately for specimens scaled geometrically. This promising characterization procedure yields cohesive laws that appear to be material properties. Such cohesive laws characterized at the coupon scale can be used to govern though-crack propagation from notches under mode I loading in large-scale structures to assess the damage tolerance.

REFERENCES

[1] Mishnaevsky Jr., L. and Brøndsted, P., 2009. "Micromechanical modeling of damage and fracture of unidirectional fiber reinforced composites: A review," *Comput. Mater. Sci.*, 44(4): 1351–1359.

[2] Rose, C. A., Dávila, C. G., and Leone, F. A., 2013. "Analysis methods for progressive damage of composite structures," *NASA/TM–2013-218024*.

[3] Wang, J. T., Poe Jr., C. C., Ambur, D. R., and Sleight, D. W., 2006. "Residual strength prediction of damaged composite fuselage panel with R-curve method," *Compos. Sci. Technol.*, 66(14): 2557–2565.

[4] Dopker, B., Murphy, D. P., Ilcewicz, L. B., and Walker, T., 1994. "Damage tolerance analysis of composite transport fuselage structure," presented at the AIAA/ASME/ASCE/AHS/ASC Structures, Structural Dynamics and Materials Conference, vol. 2, pp. 803–810.

[5] Kanouté, P., Boso, D. P., Chaboche, J. L., and Schrefler, B. A., 2009. "Multiscale Methods for Composites: A Review," *Arch. Comput. Methods Eng.*, 16(1): 31–75.

[6] "CMH-17, Materials Usage, Design and Analysis," in *Composite Materials Handbook*, vol. 2, Rev G, Philadelphia, PA: SAE; 2011.

[7] Walker, T. H., Ilcewicz, L. B., Polland, D. R., Bodine, J. B., and Poe Jr., C. C., 1993. "Tension fracture of laminates for transport fuselage. Part 3: Structural configurations," presented at the Fourth NASA/DoD Advanced Composites Technology Conference.

[8] Dugdale, D. S., 1960. "Yielding of steel sheets containing slits," *J. Mech. Phys. Solids*, 8(2): 100–104.

[9] Barenblatt, G. I., 1962. "The mathematical theory of equilibrium cracks in brittle fracture," *Adv. Appl. Mech.*, 7(1): 55–129.

[10] Hillerborg, A., Modéer, M., and Petersson, P.-E., 1976. "Analysis of crack formation and crack growth in concrete by means of fracture mechanics and finite elements," *Cem. Concr. Res.*, 6(6): 773–781.

[11] Elices, M., Guinea, G. V., Gómez, J., and Planas, J., 2002. "The cohesive zone model: advantages, limitations and challenges," *Eng. Fract. Mech.*, 69(2): 137–163.

[12] Dávila, C. G., Rose, C. A., and Camanho, P. P., 2009. "A procedure for superposing linear cohesive laws to represent multiple damage mechanisms in the fracture of composites," *Int. J. Fract.*, 158(2): 211–223.

[13] Maimi, P., Camanho, P. P., Mayugo, J.-A., and Dávila, C. G., 2006. "A Thermodynamically Consistent Damage Model for Advanced Composites," *NASA/TM-2006-214282*.

[14] Foote, R. M. L., Mai, Y.-W., and Cotterell, B., 1986. "Crack growth resistance curves in strain-softening materials," *J. Mech. Phys. Solids*, 34(6): 593–607.

[15] Cox, B. N. and Marshall, D. B., 1991. "The determination of crack bridging forces," *Int. J. Fract.*, 49(3): 159–176.

[16] Bao, G. and Suo, Z., 1992. "Remarks on Crack-Bridging Concepts," *Appl. Mech. Rev.*, 45(8): 355–366.

[17] Sørensen, B. F., and Jacobsen, T. K., 1998. "Large-scale bridging in composites: R-curves and bridging laws," *Compos. Part Appl. Sci. Manuf.*, 29(11): 1443–1451.

[18] Kongshavn, I. A., 1996. "Experimental investigation of a strain softening approach to predicting failure of notched composite laminates," MS Thesis, The University of British Columbia.

[19] Leone, F. A., Girolamo, D., and Dávila, C. G., 2012. "Progressive damage analysis of bonded composite joints," *NASA/TM–2012-217790*.

[20] Laffan, M. J., Pinho, S. T., Robinson, P., and McMillan, A. J., 2012 "Translaminar fracture toughness testing of composites: A review," *Polym. Test.*, 31(3): 481–489.

[21] Pinho, S. T., Robinson, P., and Iannucci, L., 2006. "Fracture toughness of the tensile and compressive fibre failure modes in laminated composites," *Compos. Sci. Technol.*, 66(13): 2069–2079.

[22] Laffan, M. J., Pinho, S. T., Robinson, P., and Iannucci, L., 2010. "Measurement of the in situ ply fracture toughness associated with mode I fibre tensile failure in FRP. Part I: Data reduction," *Compos. Sci. Technol.*, 70(4): 606–613.

[23] Catalanotti, G., Camanho, P. P., Xavier, J., Dávila, C. G., and Marques, A. T., 2010. "Measurement of resistance curves in the longitudinal failure of composites using digital image correlation," *Compos. Sci. Technol.*, 70(13): 1986–1993.
[24] Hou, F. and Hong, S., 2014. "Characterization of R-curve behavior of translaminar crack growth in cross-ply composite laminates using digital image correlation," *Eng. Fract. Mech.*, 117: 51-70.
[25] "ASTM Standard D5528. Test Method for Mode I Interlaminar Fracture Toughness of Unidirectional Fiber-Reinforced Polymer Matrix Composites," in *Annual Book of ASTM Standards*, vol. 15.03, W. Conshohocken, PA: ASTM Int; 2007.
[26] Rice, J. R., 1968. "A path independent integral and the approximate analysis of strain concentration by notches and cracks," *J. Appl. Mech.*, 35(2): 379–386.
[27] Yau, J. F., Wang, S. S., and Corten, H. T., 1980. "A Mixed-Mode Crack Analysis of Isotropic Solids Using Conservation Laws of Elasticity," *J. Appl. Mech.*, 47(2): 335–341.
[28] Anderson, T. L., 2005. *Fracture mechanics: fundamentals and applications*. CRC Press.
[29] Jacobsen, T. K. and Sørensen, B. F., 2001. "Mode I intra-laminar crack growth in composites — modelling of R-curves from measured bridging laws," *Compos. Part Appl. Sci. Manuf.*, 32(1): 1–11.
[30] Tamuzs, V., Tarasovs, S., and Vilks, U., 2001. "Progressive delamination and fiber bridging modeling in double cantilever beam composite specimens," *Eng. Fract. Mech.*, 68(5): 513–525.
[31] *ABAQUS Online Documentation: Version 6.12*. Providence, RI: Dassault Systèmes Simulia Corporation; 2012.
[32] Shih, C. F., Moran, B., and Nakamura, T., 1986. "Energy release rate along a three-dimensional crack front in a thermally stressed body," *Int. J. Fract.*, 30(2):. 79–102.
[33] Suo, Z., Bao, G., and Fan, B., "Delamination R-curve phenomena due to damage," *J. Mech. Phys. Solids*, 40(1): 1–16.
[34] Laffan, M. J., Pinho, S. T., Robinson, P., and Iannucci, L., 2010. "Measurement of the in situ ply fracture toughness associated with mode I fibre tensile failure in FRP. Part II: Size and lay-up effects," *Compos. Sci. Technol.*, 70(4): 614–621.
[35] Catalanotti, G., Arteiro, A., Hayati, M., and Camanho, P. P., 2014. "Determination of the mode I crack resistance curve of polymer composites using the size-effect law," *Eng. Fract. Mech.*, 118: 49–65.
[36] "ASTM Standard E2472 - 12e1. Standard Test Method for Determination of Resistance to Stable Crack Extension under Low-Constraint Conditions," in *Annual Book of ASTM Standards*, W. Conshohocken, PA: ASTM Int., 2012.
[37] "ASTM Standard E399 - 12e3. Standard Test Method for Linear Elastic Plane Strain Fracture Toughness KIc of Metallic Materials," in *Annual Book of ASTM Standards*, W. Conshohocken, PA: ASTM Int., 2012.
[38] McGowan, D. M., Ambur, D. R., and McNeil, S. R., 2003. "Full-field Structural Response of Composite Structures: Analysis and Experiment," presented at the 44th AIAA/ASME/ASCE/AHS Structures, Structural Dynamics, and Materials Conference, Norfolk, VA.